

## Corrosion behavior and mechanism of FeCoNi high-entropy alloy compared with X100 pipeline steel in a simulated alkaline soil environment

Qihang Ni, Min Zhu <sup>\*</sup>, Yongfeng Yuan, Shaoyi Guo

School of Mechanical Engineering, Zhejiang Sci-Tech University, Hangzhou 310018, China

### ARTICLE INFO

**Keywords:**  
High-entropy alloy  
X100 steel  
Corrosion behavior  
Surface film  
Inclusion

### ABSTRACT

In this work, the corrosion behavior of FeCoNi HEA and X100 pipeline steel in a simulated Golmud soil environment was systematically studied utilizing electrochemical tests, surface analysis techniques and immersion measurement. The results indicate that FeCoNi HEA possesses superior anti-corrosion property than X100 steel by comparing the charge transfer resistance ( $R_{ct}$ ), passive current density ( $i_p$ ) and corrosion morphology. The microstructure and surface film are the principal factors causing the difference in corrosion resistance of the two alloys. More intact, uniform and dense passive film enhances the anti-corrosion performance of the HEA, while the nonprotective, loose and defective corrosion product film covering the surface of X100 steel is not conducive to inhibiting the corrosion of the steel substrate. The appearance of inclusions within the HEA can generate the micro-galvanic corrosion effect with the matrix, which promotes the substrate as an anode to induce pitting. Furthermore, multiple phases of X100 steel exhibits higher electrochemical activity compared to the HEA with a single Face Center Cubic (FCC) phase, which accelerates the corrosion of the steel. Moreover, the matrix of the HEA primarily experiences selected dissolution of Ni element.

### 1. Introduction

Nowadays, high-entropy alloys (HEAs) as innovative metals have been extensively concerned, which are composed of an equal or near-equal quantity ratio materials [1–3]. HEAs possess excellent mechanical properties, which may be widely used in various industries in the future [4–6]. Among various high-entropy alloys, FeCoNi HEA with single face-centered cubic (FCC) phase is a classical multicomponent alloy with good performances [7,8]. The related researches of the HEA mainly focus on mechanical and physical properties, such as extensibility, hardness and strength, etc. [9,10]. Li et al. [11] studied the ductility performance of FeCoNi HEA analyzed by the stress-strain curve and the result indicated that its ductility (60%) was outstanding. Zuo et al. [12] pointed out that the presence of a small amount of Si content changed the phase of FeCoNi HEA from FCC to body-centered cubic (BCC) and greatly improved the yield strength (1297.1 MPa) and hardness (568 HV<sub>0.2</sub>) of the HEA. In addition, Lavakumar et al. [13] reported that using the grain refinement method could enhance the mechanical properties of FeCoNi HEA and its maximum yield strength reached 675 MPa. Therefore, it can be found that FeCoNi HEA meets the requirement of mechanical properties as a candidate material for

pipeline steel [14–17].

Besides, anti-corrosion property is a key factor affecting the service of structural materials, nevertheless, there have few studies about the corrosion behavior of HEAs [18–21]. For example, Lu et al. [22] found that the passivation region of CoCrFeMnNi HEA became wider after soaking in NaCl solution and the corrosion product film was formed on the HEA surface, which consisted of high Cr and Fe contents. Tsau et al. [23] revealed that FeCoNi HEA experienced slight corrosion in H<sub>2</sub>SO<sub>4</sub> and NaCl solutions, which suggested that the HEA had an outstanding corrosion resistance. However, the related research work on the corrosion behavior of FeCoNi HEA in an alkaline environment has not been explored.

Up to now, advanced X100 pipeline steel with good mechanical property has been increasingly applied in the long pipeline engineering field [24,25], especially in the rapidly developing northwest region of China, such as the Golmud area with alkaline soil [26,27]. For example, Duan et al. [28] studied the mechanical performance and microstructure of X100 steel and the related results revealed that the steel was composed of a multiphase structure and the yield strength of the steel reached 657 MPa. However, some researches manifested that X100 pipeline steel undergone varying degrees of corrosion in different soil

\* Corresponding author.

E-mail address: [zmii666@126.com](mailto:zmii666@126.com) (M. Zhu).

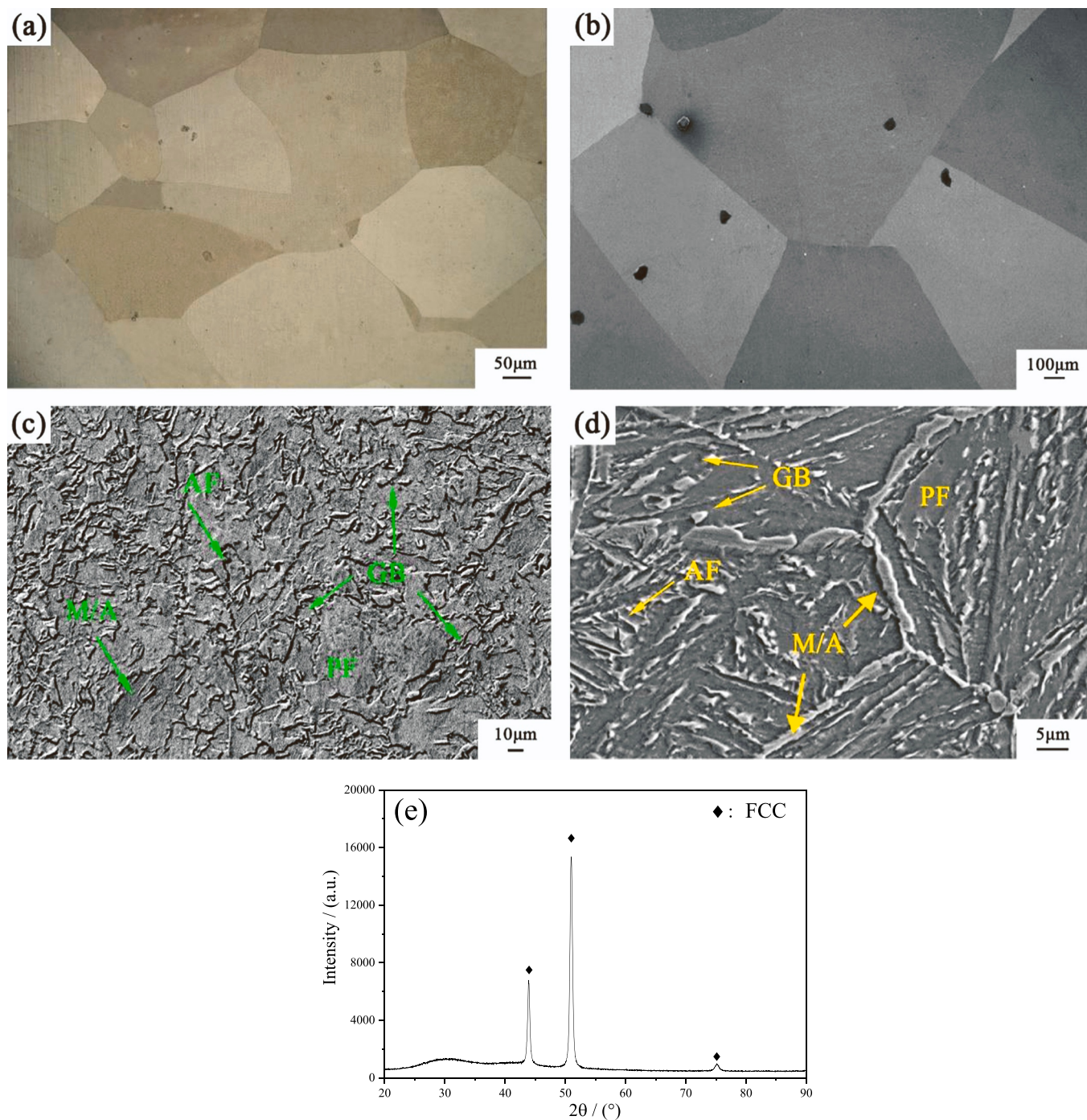


**Fig. 1.** Microstructures of FeCoNi HEA (a, b) and X100 steel (c, d), the XRD of the HEA (e).

environments [29,30]. Fu et al. [31] found that in the acidic soil solution with pH of 3.6, X100 steel possessed negative corrosion potential (-657 mV) and large corrosion current density ( $i_{\text{corr}}$  of 39.54 mA/cm<sup>2</sup>), suggesting that the corrosion rate of the steel was high. Especially in alkaline soil solution, Yang et al. [32] explored that the influence of AC density on the anti-corrosion performance of X100 steel in simulated alkaline soil environment, and the results revealed that after soaking for 96 h, general corrosion was occurred on the surface of the steel with a very serious corrosion feature, as well as the corrosion rate of the steel became significantly high with the augment of alternating current density. Wang et al. [33] found that the large  $i_{\text{corr}}$ , small passive film resistance ( $R_p$ ) and charge transfer resistance ( $R_{ct}$ ), which revealed that X100 steel possessed high pitting sensitivity in the simulated alkaline

soil environment. In addition, Zhu et al. [34] reported that plentiful pits were observed on the surface of X100 pipeline steel after the immersion test, indicating that harmful ions in the solution easily corroded the matrix of X100 steel. Consequently, there is a serious risk of corrosion when X100 steel is employed in the Golmud area. Thus, in search of a new metal with exceptional corrosion resistance to replace X100 pipeline steel, it is necessary to carry out the comparative study of corrosion behavior between FeCoNi HEA and X100 pipeline steel in the Golmud soil environment, which can provide a reference for the HEA applied in the pipeline engineering field.

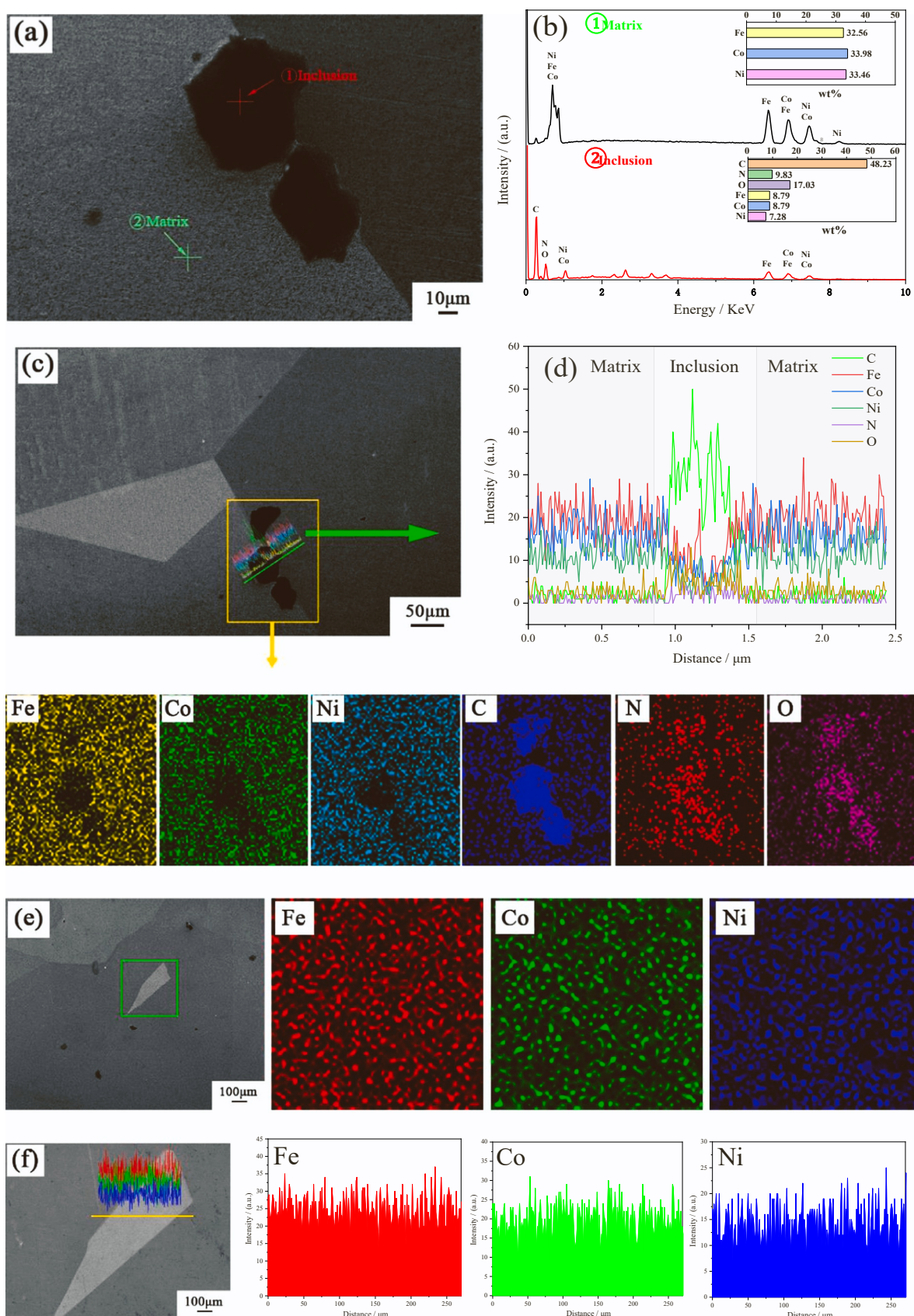


**Fig. 2.** The EDS results of inclusion (a-d) and matrix (e,f) of FeCoNi HEA.

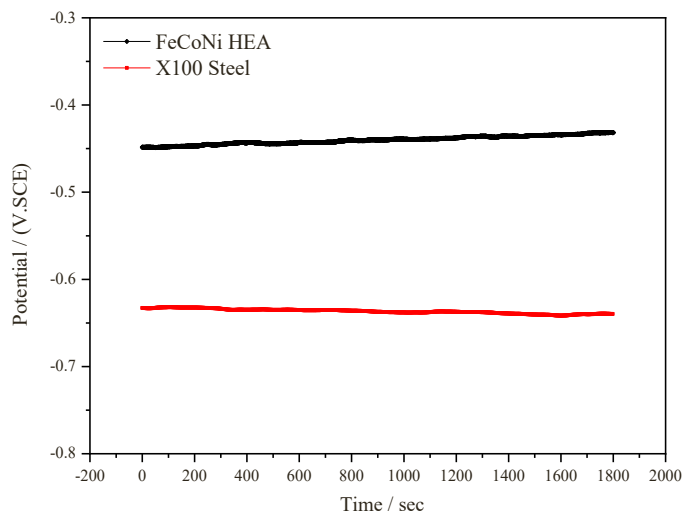


Fig. 3. Open circuit potential of FeCoNi HEA and X100 steel.

## 2. Experimental

### 2.1. Material and solution

The equiatomic FeCoNi HEA was fabricated by the high-purity raw materials of Fe, Co and Ni in an induction suspension furnace at 1700°C under the argon atmosphere, and then cooled in the furnace for 30 minutes to ambient temperature. To ensure the uniform distribution of elements, the specimen was required to be remelted four times and cut into 10 mm×5 mm×3 mm, followed by degreasing, washing, and drying. Subsequently, the HEA sample was sealed with epoxy resin and ground respectively with sandpapers from 180 to 2000 grit. The chemical composition (wt%) of X100 pipeline steel (hot-rolled) prepared by Magang (Group) Holding Co., Ltd. was C 0.04, Si 0.20, Mn 1.55, Mo 0.02, Al 0.02, Cu 0.25, Ni 0.13, Ti 0.02, Nb 0.052, Cr 0.016 and Fe balance, as well as the HEA consisted of Fe 32.56, Co 33.98 and Ni 33.46. In this work, the solution containing 11.34% Cl<sup>-</sup>, 0.262% SO<sub>4</sub><sup>2-</sup> and 0.0099% HCO<sub>3</sub><sup>-</sup> with pH of 9 was used to simulate the Golmud alkaline soil environment. All tests were conducted at a constant temperature (35°C).

### 2.2. Microstructural analysis

The ground HEA and X100 steel samples were polished with 0.5 μm

diamond paste. The HEA was etched by using the aqua regia, then cleaned with alcohol and deionized water, as well as dried with cold air. For X100 steel, its etchant was 4% nital (4 mL nitric acid and 96 mL ethanol). Afterward, the microstructure characteristics of the two alloys were analyzed via stereomicroscope (VHX-2000 C), scanning electron microscope (SEM, FEI-quanta 250) and energy dispersive spectrometer (EDS). The grain size of the HEA was statistically calculated via the linear intercept method. Moreover, the phase composition of the HEA was measured by X-ray diffraction (XRD, Shimadzu 6000, Cu-target).

### 2.3. Electrochemical tests

The electrochemical tests of the HEA and X100 steel were performed by a CHI660E electrochemical workstation equipped with the conventional three-electrode system. The samples of the two alloys were employed as the working electrode (WE), the platinum plate was applied as the counter electrode (CE), and the saturated calomel electrode (SCE) acted as the reference electrode (RE). Before testing, the two alloys were immersed in the solution for 0.5 h. And then, the electrochemical impedance spectroscopy (EIS) was tested with a signal amplitude of 10 mV in the frequency range of 100 kHz to 10 mHz after the open circuit potential (OCP) for 30 minutes. The equivalent electrical circuit (EEC) was adopted to fit the impedance data by ZsimWin software. Subsequently, the potentiodynamic polarization curve test was conducted with a scanning rate of 0.5 mV/s in a potential range of -1 V (vs. SCE) to 0 V (vs. SCE). In addition, The Mott-Schottky curve was measured at a fixed frequency of 1 kHz starting from -0.8 V to 0.2 V (vs. SCE), and the step length was 50 mV. Prior to testing, the two alloys were finely ground and polished, then the passive film of the HEA was prepared at a constant passive potential of -0.23 V (vs. SCE) by potentiostatic polarisation for 2 h, as well as the surface film of X100 steel was formed by immersion for 2 h. All tests were conducted more than four times to guarantee experimental reproducibility by using multiple samples.

Table 1

The fitted results for potentiodynamic polarization curves of FeCoNi HEA and X100 steel in Golmud soil simulated solution.

Alloys	$i_{corr}$ ( $10^{-6} A \cdot cm^{-2}$ )	$E_{corr}$ (V)	$E_p$ (V)	$i_p$ ( $10^{-6} A \cdot cm^{-2}$ )
FeCoNi HEA	4.256	-0.428	-0.129	3.328
X100 steel	14.4	-0.725	—	—

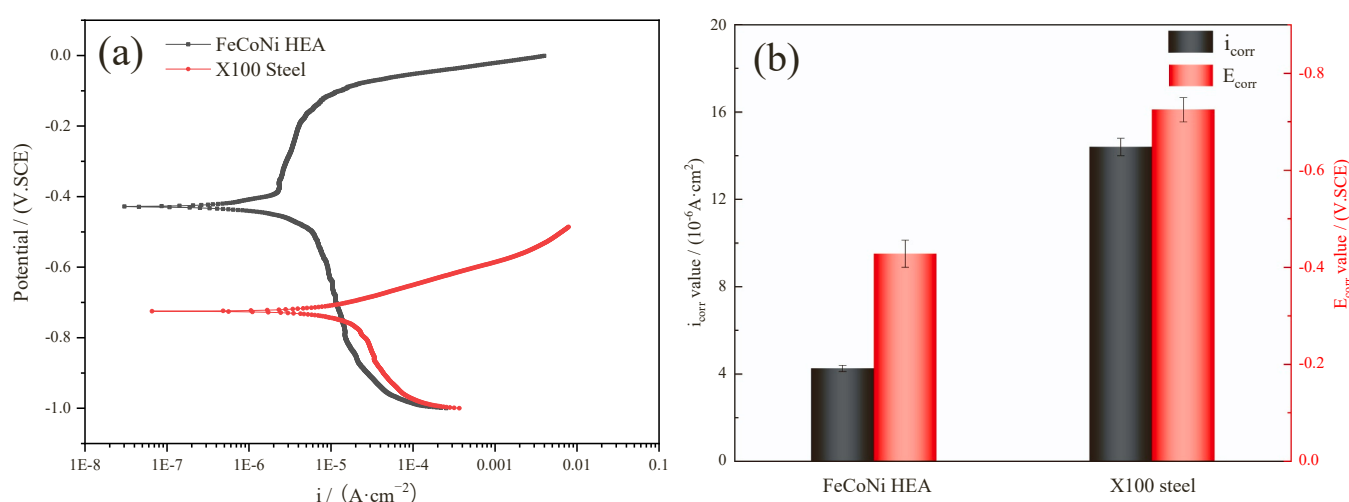
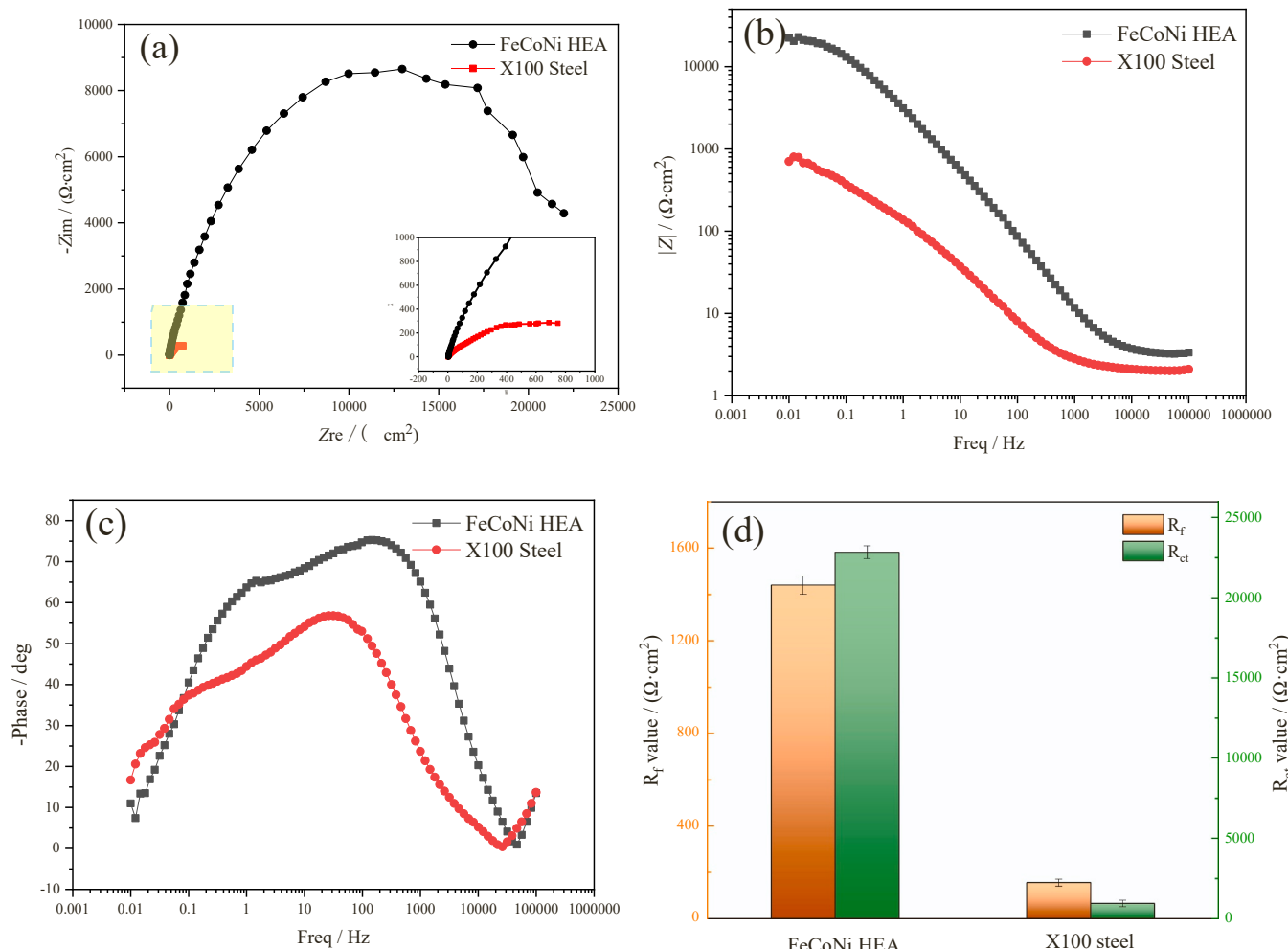
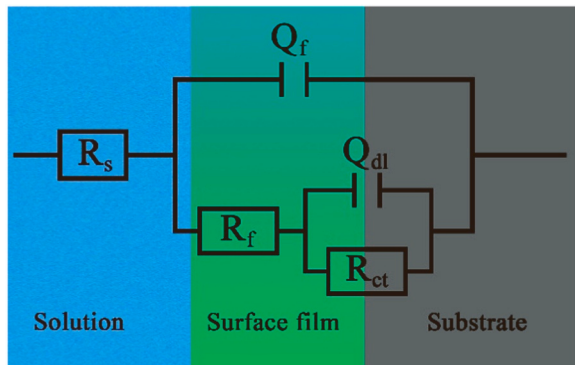


Fig. 4. Potentiodynamic polarization curves (a) and the related results (including  $i_{corr}$  and  $E_{corr}$  values) (b) of FeCoNi HEA and X100 steel.



**Fig. 5.** EIS curves of the HEA and X100 steel in a simulated Golmud soil environment: (a) Nyquist plots; (b, c) Bode plots, and (d) the fitted data of  $R_f$  and  $R_{\text{ct}}$ .



**Fig. 6.** Equivalent circuit model used for fitting EIS data.

#### 2.4. AFM analysis

For further study of the morphology characteristics of surface films covered on the HEA and X100 steel, which were analyzed by an atomic force microscope (AFM, PSLA XE-100 E). Before testing, the surface films of the two alloys were produced as the procedures described in the Mott-Schottky curve.

#### 2.5. Immersion and XPS test

The HEA and X100 steel were ground, polished, rinsed, dried and weighed. Then the two alloys were soaked in the simulated alkaline soil solution for 6 days. After testing, all the samples were removed the surface rust, washed and dried. The derusting solution of the HEA was 5% dilute nitric acid, and the rust removing solution consisted of 500 mL ultrapure water, 500 mL HCl and 3.5 g hexamethylenetetramine was used to remove the surface corrosion product of the steel. Subsequently, the corrosion morphology was observed through the SEM and EDS, and the loss of weight was used to calculate the average corrosion rate. Besides, the corrosion morphology of X100 steel was analyzed by the

**Table 2**

The fitted electrochemical parameters for EIS diagrams of FeCoNi HEA and X100 steel in Golmud soil simulated solution.

Alloys	$R_s$ ( $\Omega \cdot \text{cm}^2$ )	$Q_f$ ( $10^{-5} \Omega^{-1} \cdot \text{cm}^{-2} \cdot \text{s}^{-n}$ )	$R_f$ ( $\Omega \cdot \text{cm}^2$ )	$n_1$	$Q_{\text{dl}}$ ( $10^{-5} \Omega^{-1} \cdot \text{cm}^{-2} \cdot \text{s}^{-n}$ )	$R_{\text{ct}}$ ( $10^4 \Omega \cdot \text{cm}^2$ )	$R_p$ ( $10^4 \Omega \cdot \text{cm}^2$ )	$C_{\text{eff}}$ ( $10^{-6} \text{F} \cdot \text{cm}^{-2}$ )	d (nm)
FeCoNi HEA	3.344	3.413	1440	0.885	4.718	2.284	2.428	9.55	1.012
X100 steel	2.03	107.9	158.5	0.861	282.7	0.101	0.116	—	—

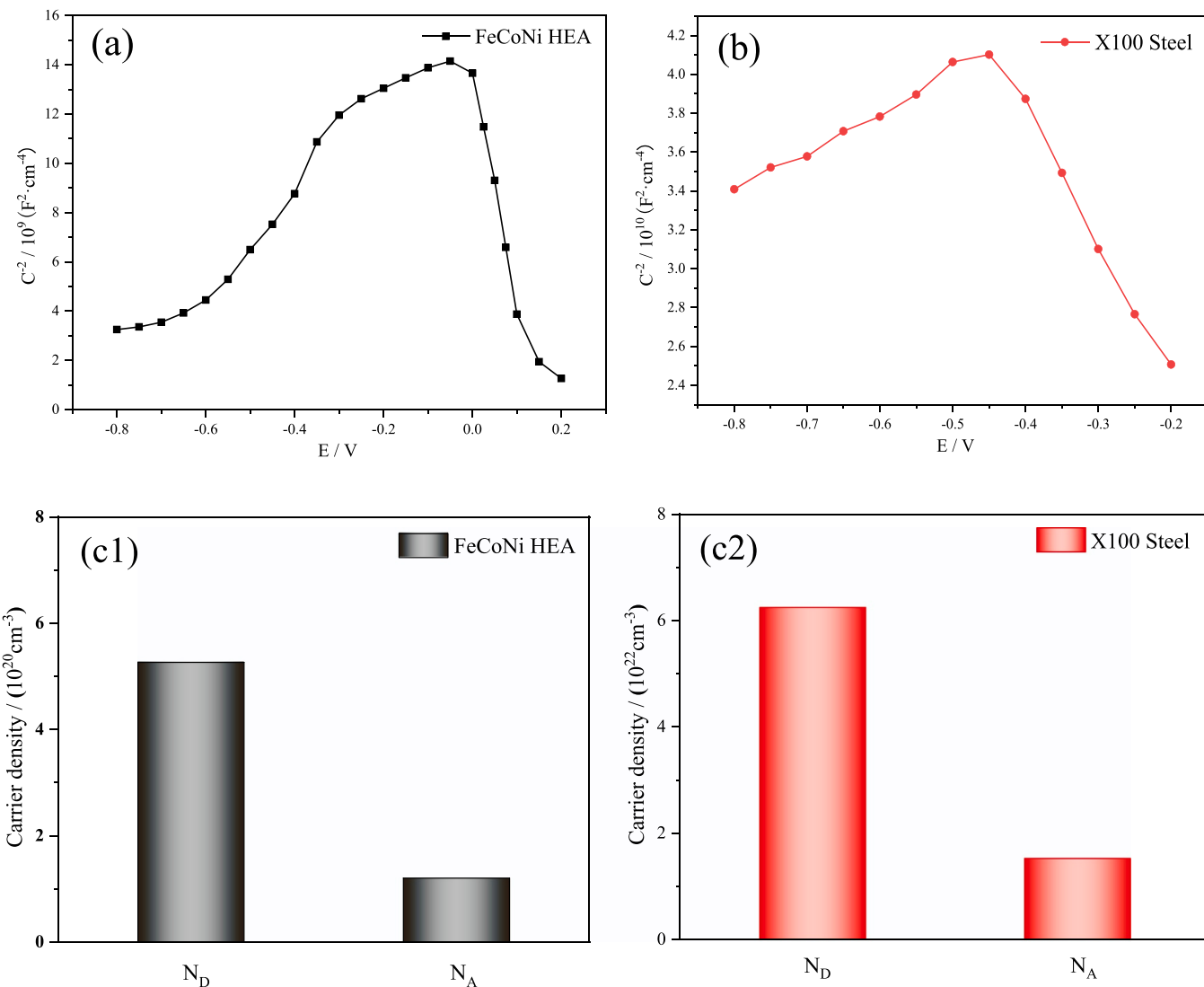


**Fig. 7.** Mott-Schottky plots of FeCoNi HEA and X100 steel (a,b), carrier densities of the surface films formed on the HEA and X100 steel (c1,c2).

stereomicroscope.

The composition of the HEA after immersion corrosion was measured via X-ray photoelectron spectroscopy (XPS) with a monochromatic Al-K $\alpha$  excitation source (USA, Thermo Fisher Scientific). The binding energies were calibrated by the standard C1s peak (284.8 eV). And the spectra data were analyzed through Xpspeak (version 4.1) software.

### 3. Results and discussion

#### 3.1. Microstructure analysis

As seen in Fig. 1, FeCoNi HEA consists of a single Face Center Cubic (FCC) phase (Fig. 1e) and its average grain size is measured as 519.1  $\mu\text{m}$ . Moreover, few black particles are sporadically distributed on the surface of the HEA (Fig. 1(a,b)). According to the related EDS analysis, the particles with a polygonous shape are inclusions containing C, N, O, Fe, Co and Ni elements, as well as the HEA substrate is composed of nearly equal weight mass ratio Fe, Co and Ni elements (Fig. 2(a-d)). Obviously, the HEA matrix has higher contents of Fe, Co and Ni in comparison with the inclusion. Among them, the existence of C, N and O elements in the inclusions of the HEA may be due to metallurgical pollution from impurities inside the industrial-grade raw metals [35]. Furthermore, the

EDS results of line scanning and mapping analysis in Fig. 2(e,f) suggest that the Fe, Co and Ni elements are uniformly distributed in the internal of grain and at the grain boundary.

By contrast, multiple phases are found in X100 pipeline steel [36]. The microstructure of the steel displays that it contains plentiful acicular ferrite (AF) with small and irregular grain. The grain boundaries are blurred, incomplete and discontinuous. A little amount of large polygonal ferrite (PF), some granular bainite (GB) and bright white M/A island can be clearly seen at grain boundary region (Fig. 1(c,d)). Notably, the grain size of X100 steel is significantly smaller than that of the HEA.

#### 3.2. Electrochemical measurements

Fig. 3 displays the open circuit potential (OCP) of FeCoNi HEA and X100 pipeline steel. Both the OCP of the two alloys remain stable during the testing time. The stable potential value of the HEA (i.e., -442.5 mV) is more positive than X100 steel (i.e., -635.5 mV), which means that the HEA possesses a lower corrosion tendency compared with the steel [37]. The potentiodynamic polarization curves of the two alloys are exhibited in Fig. 4a. The shape of the two curves is similar in the cathode region, which suggests that the alloys with different element contents have a relatively small effect on the cathode process [38]. Obviously, the classic passive region is found in the anodic curve of the HEA without

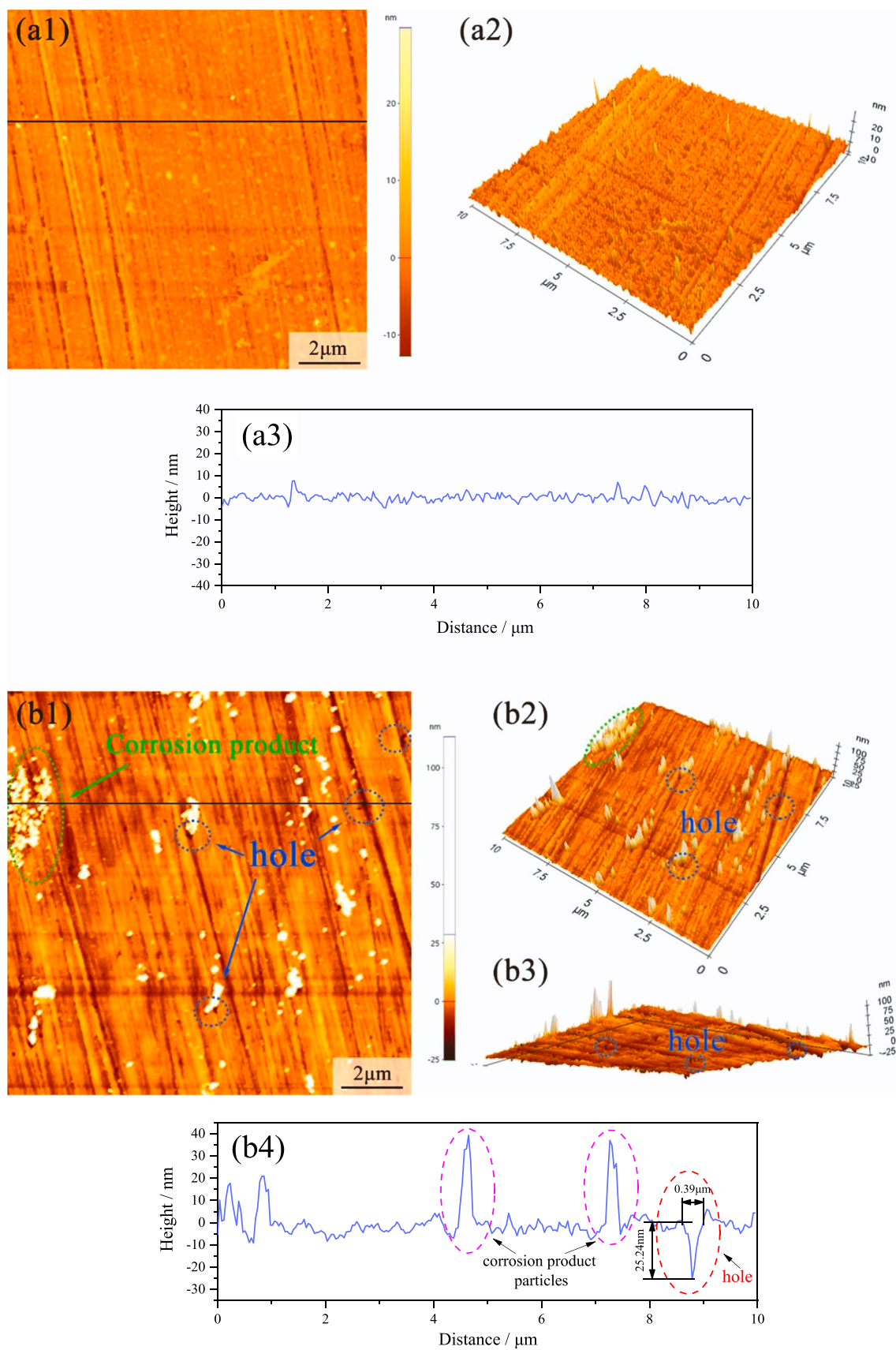


**Fig. 8.** The topography morphologies of surface films formed on the HEA (a1-a3) and X100 steel (b1-b4) in a simulated Golmud soil environment.

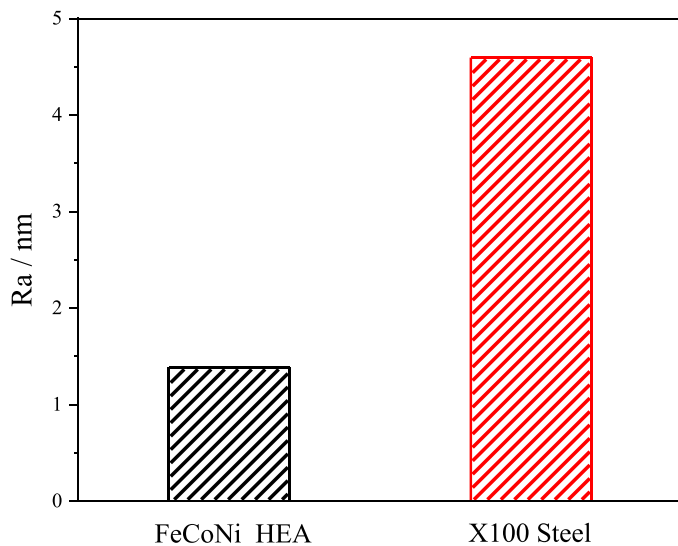


**Fig. 9.** Roughness of FeCoNi HEA and X100 pipeline steel.

active-passive transition zone, revealing that the spontaneous passivation of the HEA occurs in the simulated alkaline soil solution with high  $\text{Cl}^-$  content [39]. Whereas X100 steel displays a significant activation characteristic, which indicates that the steel undergoes active anodic dissolution and corrosion product film is formed on its surface. Generally, the protection capability of the corrosion product film is distinctly worse than that of the passive film. Thus, the passive film of the HEA can enhance the corrosion resistance of the substrate. The corresponding fitting parameters of polarization curve of the two alloys, including the pitting potential ( $E_p$ ), corrosion potential ( $E_{\text{corr}}$ ), corrosion current density ( $i_{\text{corr}}$ ) and passive current density ( $i_p$ ), are given in Table 1. The  $E_{\text{corr}}$  values of the HEA and X100 steel, which are extrapolated from the linear section of the Tafel slope [40]. In Fig. 4b, the more negative  $E_{\text{corr}}$  value of X100 steel implies its larger corrosion tendency [41]. Apparently, the  $i_{\text{corr}}$  value of X100 steel is larger than three times that of the HEA. Qiu et al. [42] reported that the lower  $i_{\text{corr}}$  value suggested the smaller corrosion rate. Therefore, the HEA exhibits more outstanding anti-corrosion property than X100 steel. In addition, the curve of the

HEA is located on the left of X100 steel, combined with the low  $i_p$  ( $3.328 \mu\text{A}\cdot\text{cm}^{-2}$ ) and high  $E_p$  (-0.129 V). This reflects that the surface of the HEA is covered by a relatively stable and protective passive film, which significantly improves the corrosion resistance of FeCoNi HEA.

The EIS curves of FeCoNi HEA and X100 steel are shown in Fig. 5. The analogous capacitive arc characteristics of the two alloys are presented in the Nyquist plot of Fig. 5a. It is universally acknowledged that the anti-corrosion performance of the HEA and X100 steel can be reflected by the radius of capacitive arc. Obviously, the radius of semi-circular arc of the HEA is larger than that of X100 steel, revealing that the interface between passive film and the matrix of the HEA possesses a higher charge transfer resistance ( $R_{\text{ct}}$ ) [43,44]. Ravindranath et al. [45] found that high frequency resulted in non-linear influence subduing the polarization resistance ( $R_p$ ). Consequently, selecting a low frequency could effectively ensure the accuracy of  $R_p$ . Moreover, Nishikata et al. [46] studied that in the frequency area lower than 1 kHz with phase angle larger than  $45^\circ$ , the current distribution became even, which revealed that the impedance at a low frequency (0.01 Hz) corresponded to the precise polarization resistance. As shown in Fig. 5b, a greater  $|Z|$  value at 0.01 Hz implies that the HEA has superior corrosion resistance to X100 steel in a simulated alkaline soil solution. In addition, a difference in the maximum phase angle (Fig. 5c) also reveals different corrosion performances of the two alloys. In particular, the utmost phase angle of the HEA reaches  $75^\circ$ , which reflects that a stable passive film is produced on the surface of the HEA, whereas the phase angle of the steel is below  $60^\circ$  and the range of high phase angle is narrower than that of the HEA, suggesting that the stability and protection of the corrosion product film covering the surface of X100 steel is relatively poor [47, 48]. Combined with the Bode plot in Fig. 5c, the EIS curve presents two time constants and different slopes, which may be attributed to the formation of surface film on the two alloys and the electrochemical response of the electric double layer [49].

To further investigate the difference in corrosion resistance of the two alloys, the EIS data are analyzed through the equivalent electrical circuit (EEC) in Fig. 6, where  $R_s$  denotes the solution resistance,  $R_f$  symbolizes the surface film resistance,  $Q_f$  represents the capacitance of the surface film,  $R_{\text{ct}}$  is the charge transfer resistance and  $Q_{\text{dl}}$  corresponds the non-ideal electric double layer capacitance. Furthermore, the  $R_p$  reflects the corrosion rate of metal alloys, which can be calculated by the sum of  $R_{\text{ct}}$  and  $R_f$  values (Formula 1), as well as the fitting results are

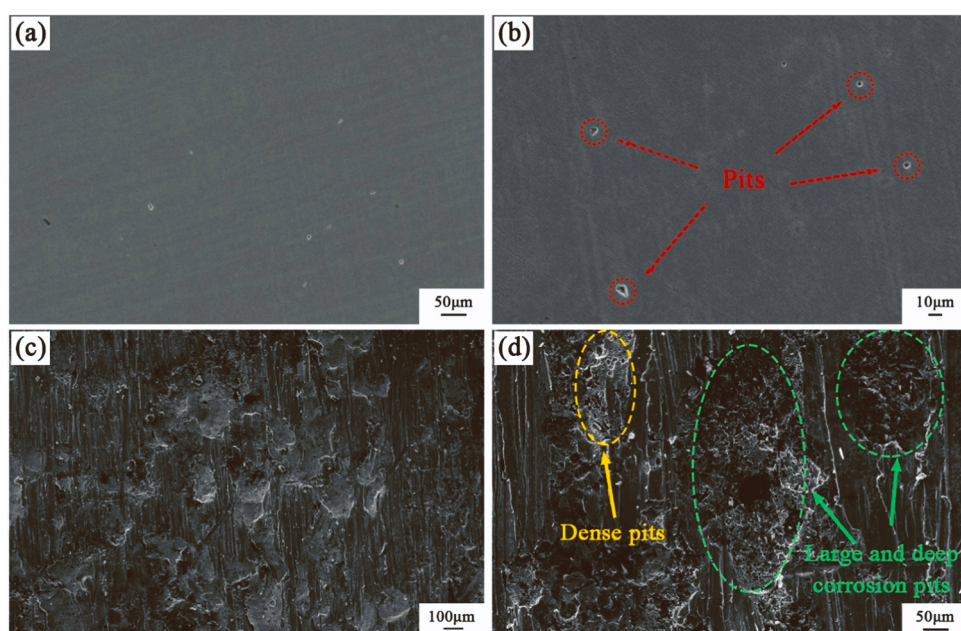


**Fig. 10.** Corrosion morphologies of FeCoNi HEA (a,b) and X100 steel (c,d) immersed for 6d after derusting.

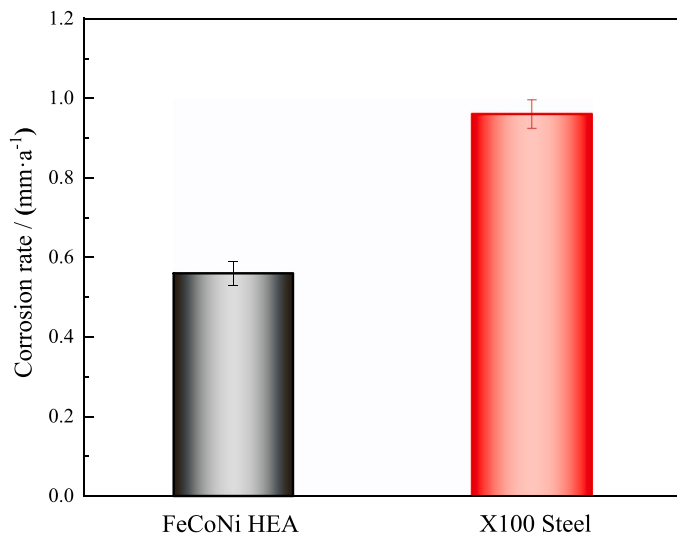


**Fig. 11.** Average corrosion rates of FeCoNi HEA and X100 steel after immersion test.

presented in Table 2 and Fig. 5d. The larger  $R_{ct}$  and lower  $Q_f$  values of FeCoNi HEA in comparison with X100 steel suggest that a denser and lower defect density passive film is produced on the HEA, which

effectively decreases the electrochemical reaction rate, and enhances the corrosion resistance of the HEA. In addition, the relatively small  $R_f$  value of the two alloys is attributed to the high content of  $\text{Cl}^-$  in the simulated alkaline soil solution. But even so, the  $R_f$  value of the HEA is nearly an order of magnitude larger than that of the steel, which manifests that a more protective and stable passive film is covered on the surface of the HEA and significantly inhibits the erosion of detrimental ions in the solution [50]. Consequently, combined with the result of polarization curve, the anti-corrosion performance of the HEA is more outstanding than that of the steel.

$$R_P = R_f + R_{ct} \quad (1)$$

Moreover, the thickness (d) of passive film covering the HEA can be measured by the corresponding EIS fitting data (Formula 2):

$$d = \frac{\epsilon \epsilon_0}{C_{eff}} \quad (2)$$

where  $\epsilon$  represents the relevant permittivity of passive film, for the HEA, its value is 12 [51,52].  $\epsilon_0$  represents the vacuum permittivity ( $8.854 \times 10^{-12} \text{ F} \cdot \text{m}^{-1}$ ) and  $C_{eff}$  is the effective capacitance of passive film, which can be acquired by Formula 3 [53]. Among them, n symbolizes the exponent of the film capacitance. And the calculated thickness of passive film on the HEA (1.012 nm) is given in Table 2.

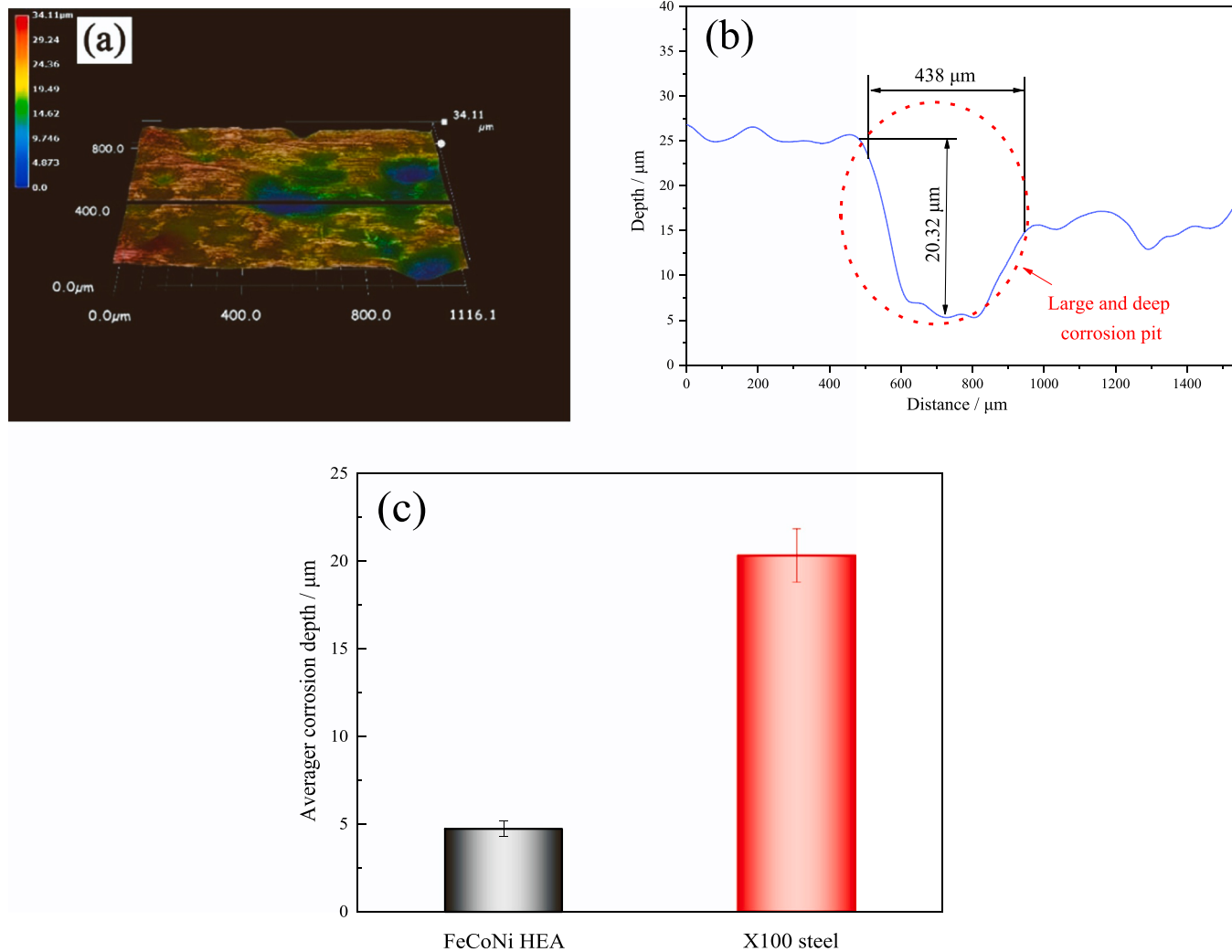


**Fig. 12.** 3D morphology of X100 steel immersed for 6d (a), the corresponding data (b) and the average corrosion depth of the two alloys (c).

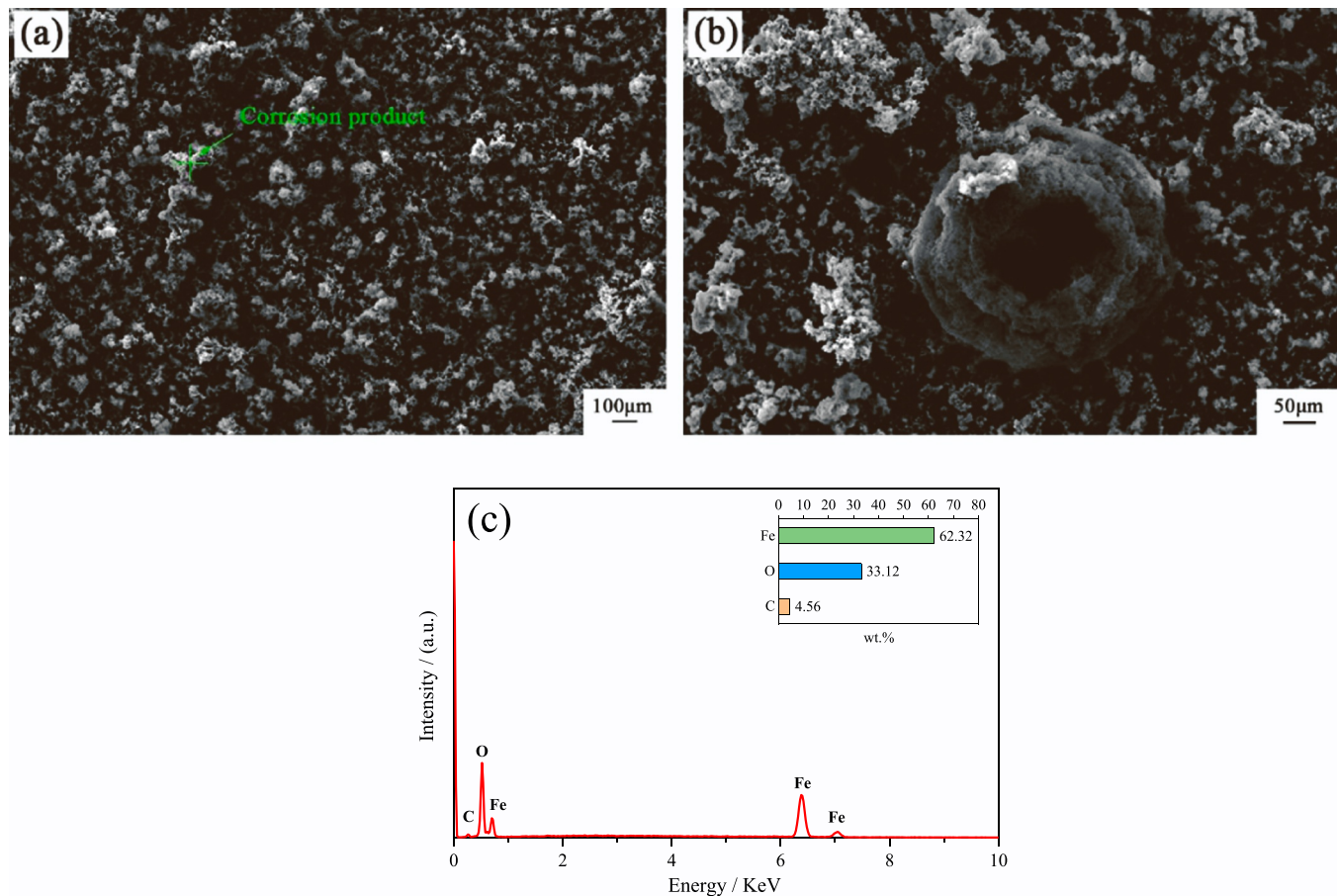


**Fig. 13.** Morphologies (a,b) and EDS result (c) of corrosion products on X100 steel.

$$C_{eff} = \left( Q_f \right)^{\frac{1}{n}} \left( \frac{1}{R_s} + \frac{1}{R_{ct}} \right)^{\frac{n-1}{n}} \quad (3)$$

Generally, surface films grown on the surface of alloys exhibit semiconductor property. In this work, using the Mott-Schottky method explores the semiconductor behavior of surface films formed on FeCoNi HEA and X100 steel. The correlation between the space charge capacitance ( $C$ ) and the applied electrode potential ( $E$ ) is shown in the following equation (Formula 4) [54,55]:

$$\frac{1}{C^2} = \pm \frac{2}{eN\epsilon\epsilon_0} \left( E - E_{FB} - \frac{kT}{e} \right) \quad (4)$$

where  $\epsilon$  represents the dielectric constant of surface film, in this work,  $\epsilon$  values of the HEA and X100 steel are 12 and 15.6, respectively [51,52,56],  $\epsilon_0$  is the vacuum permittivity ( $8.854 \times 10^{-12} \text{ F}\cdot\text{m}^{-1}$ ),  $e$  denotes the electronic charge ( $1.602189 \times 10^{-19} \text{ C}$ ),  $N$  is the carrier density,  $K$  symbolizes the Boltzmann constant ( $1.38 \times 10^{-23} \text{ J/K}$ ), and  $T$  is the absolute temperature (K).  $E$  is the applied electrode potential, and  $E_{FB}$  describes the flat-band potential.

**Fig. 7(a,b)** shows the Mott-Schottky curves of the HEA and X100 steel, both of which possess n-p semiconductor characteristics. In the applied potential range, the two linear areas (positive and negative slopes) represent the different electronic structures of the surface film formed on the two alloys. According to the previous reports, the composition of the surface film plays a key role in the n-p type response. And the surface film is composed of the inner and outer layers, which is related to p-type and n-type characteristics, respectively [57–59]. Among them, the oxides of Ni and Co elements are regarded as p-type semiconductor, as well as the n-type semiconductor characteristic can be reflected by iron compounds [60–62]. Additionally, the negative sign

expresses the p-type semiconductor of surface film, which contains the main defects of cation vacancies. The semiconductor property transforms to the n-type on the basis of the positive sign with the primary defects of oxygen vacancies or cation interstitials.

The calculated values of  $N_A$  (acceptor density) and  $N_D$  (donor density) of the two alloys are shown in **Fig. 7(c1, c2)**, which are applied to further explore the semiconductive property of the surface film. The  $N_A$  and  $N_D$  values of the HEA are two orders of magnitude smaller than those of X100 steel, revealing that the passive film of the HEA is more compact, intact and stable, which defends harmful ions to permeate the substrate, and improves the protective ability of the HEA matrix [63]. Besides, on account of point defect model (PDM) [64–66], the higher  $N_D$  value of X100 steel is due to the defective and nonprotective corrosion product film formed on the surface of the steel, enhancing the initiation and growth of corrosion pits. Thus, compared with X100 steel, the HEA has superior corrosion resistance, which is in accord with the result of polarization curve and EIS data.

### 3.3. AFM analysis

To deeply compare the difference in surface films of FeCoNi HEA and X100 pipeline steel, AFM measurement was used to analyze the topography characteristics of surface films covering the two alloys. In **Fig. 8 (a1-a3)**, passive film grown on the surface of the HEA is relatively complete, dense and uniform with a mild height fluctuation along the intercept line, which effectively protects the HEA matrix from corrosion. In contrast, numerous white particles and large height fluctuation are evidently observed for the steel (**Fig. 8 (b1-b4)**). Combining the results of EIS and polarization curves, the uneven, discontinuous and loose surface film with random distribution of white particles is corrosion

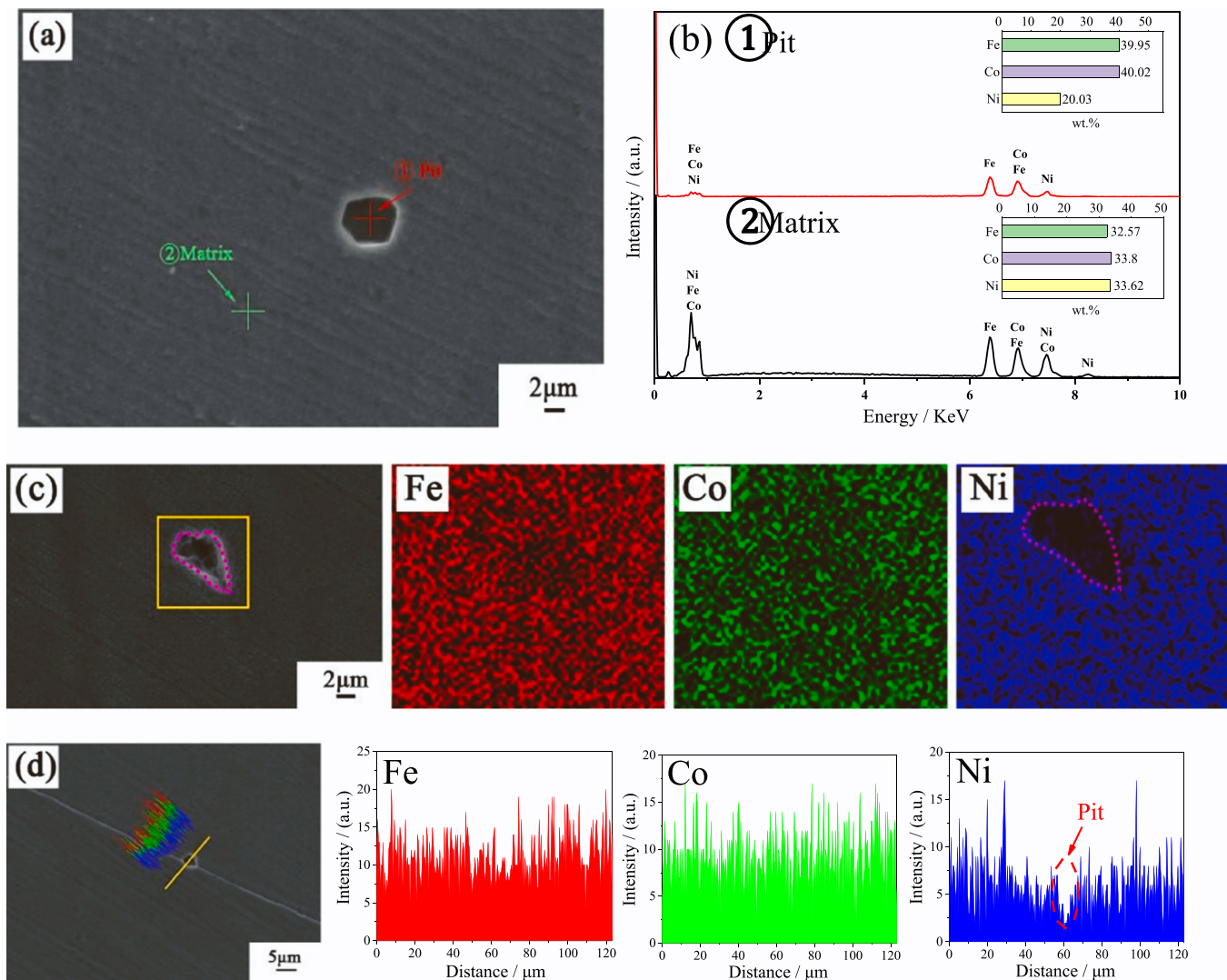


**Fig. 14.** Morphologies and EDS analysis of pits on FeCoNi HEA after immersion test.

product film, which benefits to providing channels for harmful ions to corrode the substrate of the steel. Moreover, the morphology of the corrosion product film on the steel presented in Fig. 13 directly verifies this view. In addition, as shown in Fig. 9, the larger roughness of X100 steel is about 4.596 nm in comparison with the Ra value (1.386 nm) of the HEA. Katkar et al. [67] found that more harmful ions easily adsorbed on the rougher film of alloys. Hence, the accumulation of deleterious ions and molecules in the heterogeneous regions of the corrosion product film formed on the surface of the steel, which promotes the occurrence of pitting corrosion. Therefore, FeCoNi HEA possesses more excellent corrosion resistance compared with X100 steel.

#### 3.4. Immersion test

Fig. 10 displays the corrosion morphologies of FeCoNi HEA and X100 pipeline steel after soaking for 6 d. Few pinhole pits are sporadically distributed on the surface of the HEA in Fig. 10 (a,b), suggesting a slight corrosion status. On the contrary, in Fig. 10 (c,d), X100 steel experiences severe uniform corrosion. The surface of the steel is rugged with numerous corrosion pits. In local regions, dense pits of different sizes are produced, and some part of them fuse into large and deep corrosion pits, revealing that the surface corrosion product film covering on the steel has low protection. Besides, plentiful small pits are inside of large corrosion pits. In addition, as shown in Fig. 11, the average corrosion

rate of the HEA is significantly smaller than that of the steel. Consequently, on the basis of corrosion morphology and corrosion rate, FeCoNi HEA possesses superior anti-corrosion property.

To directly reflect the corrosion state of X100 steel, its 3D morphology was measured by stereomicroscope. The steel suffers serious general corrosion with apparently uneven characteristics, as well as a large corrosion pit with depth of 20.32 μm and width of 438 μm (Fig. 12a,b) is observed. As shown in Fig. 12c, in comparison with FeCoNi HEA, the average pit depth of the steel is more than four times that of the HEA, which proves the severe corrosion of the steel again.

Fig. 13 shows the morphology and EDS result of corrosion product formed on X100 steel. The incomplete and uneven corrosion product film with many holes is exhibited in Fig. 13a. Under high magnification, large holes exist in the corrosion product (Fig. 13b), revealing that the corrosion product film grown on the surface of the steel is loose, porous and defective. Moreover, the corresponding EDS result indicates that the surface film mainly contains Fe, O and C elements (Fig. 13c). As is well known, the stability and protectiveness of iron oxides are relatively low [68]. Combined with the corrosion morphology presented in Fig. 10(c, d) and Fig. 12(a, b), it is demonstrated that the corrosion product film of the steel has poor protection performance, which cannot effectually restrain the steel matrix from being corroded.

For the HEA, to deeply analyze the formation mechanism of pitting corrosion, the internal composition of pits was measured by the EDS

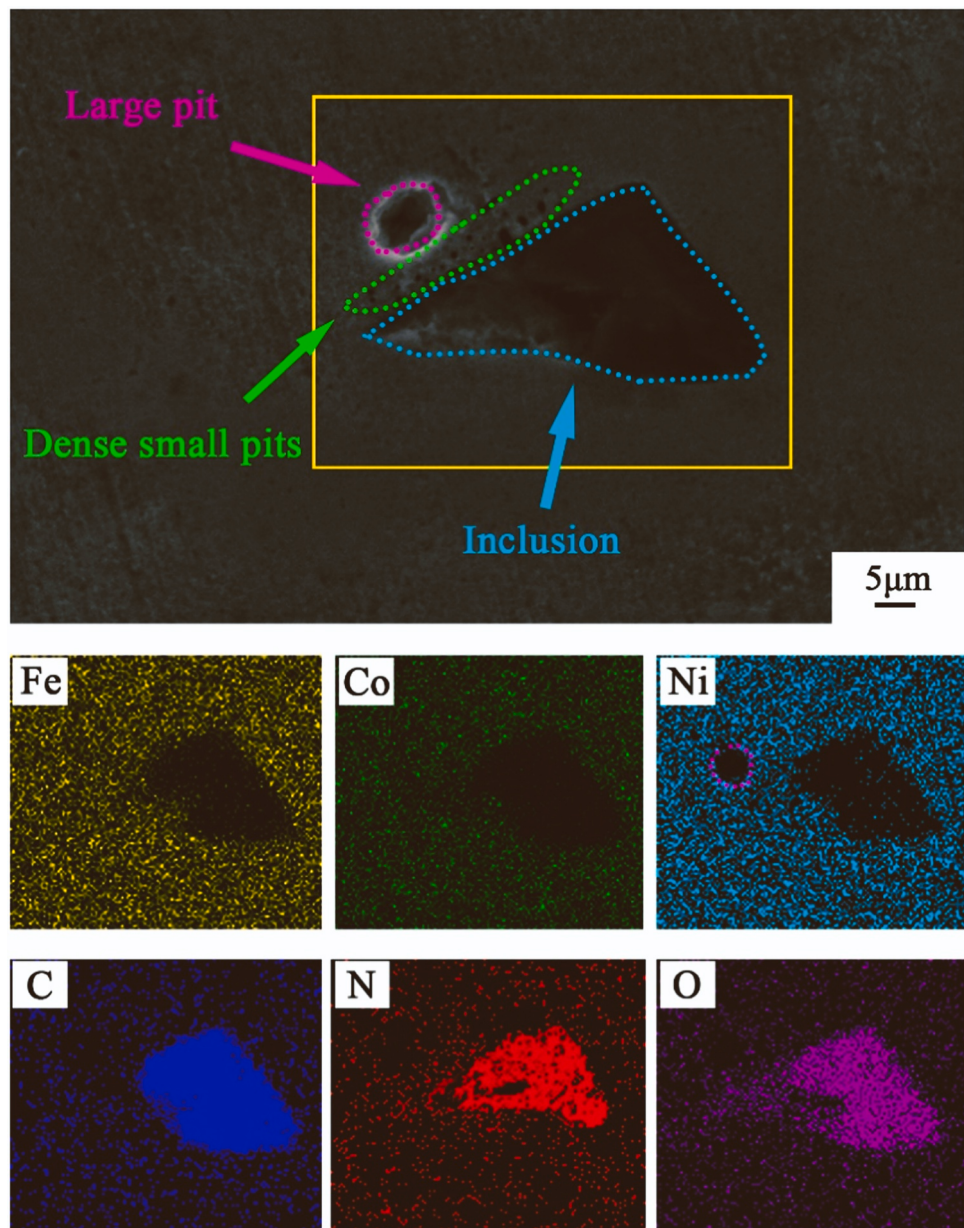


**Fig. 15.** Morphology and EDS result of inclusion on the surface of FeCoNi HEA after immersion test for 6d.

(including point scanning, line scanning and mapping). As displayed in Fig. 14(a,b), compared with the HEA substrate, the content of Ni element inside the pit is significantly reduced, suggesting that the dissolution of Ni element occurs in the pit region (Eq. 1). Moreover, since the EDS results provide the relative composition, it is possible that other elements (Fe and Co) are also dissolved inside pits (Eqs. 2–5) but at a relatively slower rate compared to the Ni element, which can be reflected by the significant decrease of Ni content inside pit. Consequently, the HEA matrix experiences element dissolution, particularly the selective dissolution of Ni element. Furthermore, the EDS line-scanning and mapping results in Fig. 14(c,d) demonstrate that the pit formed on the HEA is mainly caused by the dissolution of Ni element.

In addition, the EDS mapping result shown in Fig. 15 in comparison with the original data in Fig. 2(a-d) indicates that the black triangular particle is the inclusion, and the large pit occurs near the inclusion. In addition, dense small pits are produced at the interface region between the HEA substrate and the inclusion due to its relatively high energy. Also, the selective dissolution of Ni element inside the large pit is

verified again via the EDS result. This phenomenon reveals that the pit located around the inclusion is attributed to the micro-galvanic corrosion between the HEA matrix and inclusion [69]. Among them, the inclusion is acted as the cathode (Eq. 6) while the substrate of the HEA serves as the anode, which accelerates the corrosion of the HEA. Moreover, it can be found that the inclusion after immersion test is incomplete, although it acts as the cathode part in the micro-galvanic corrosion cell, the inclusion within the HEA dissolves itself. Known from the literature on the similar alloy of CoCrFeMnNi HEA [70]. To further explore the composition of the corroded HEA after immersion for 6d, the XPS test was conducted. Fig. 16 exhibits the XPS spectra of Fe 2p<sub>3/2</sub>, Co 2p<sub>3/2</sub> and Ni 2p<sub>3/2</sub> of the HEA and the binding energies are referred to the related literature [71,72]. The results indicate that both iron and cobalt exist in two types of divalent and trivalent states, as well as only a divalent state is presented for Ni element. Based on the above analysis, the possible electrochemical reactions are as follows:

Dissolution of the HEA matrix:



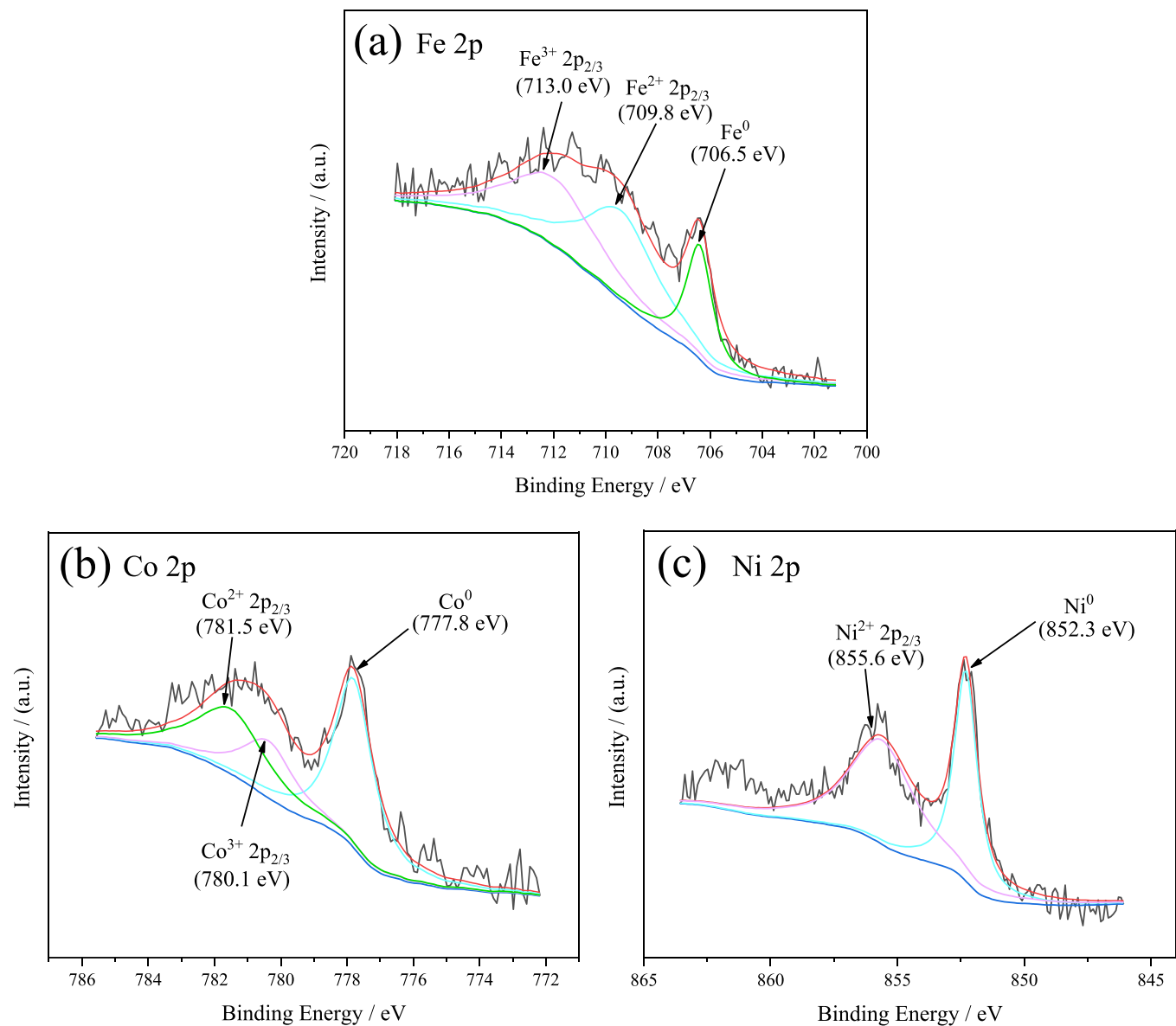


Fig. 16. XPS spectra of corroded HEA after immersion for 6d.

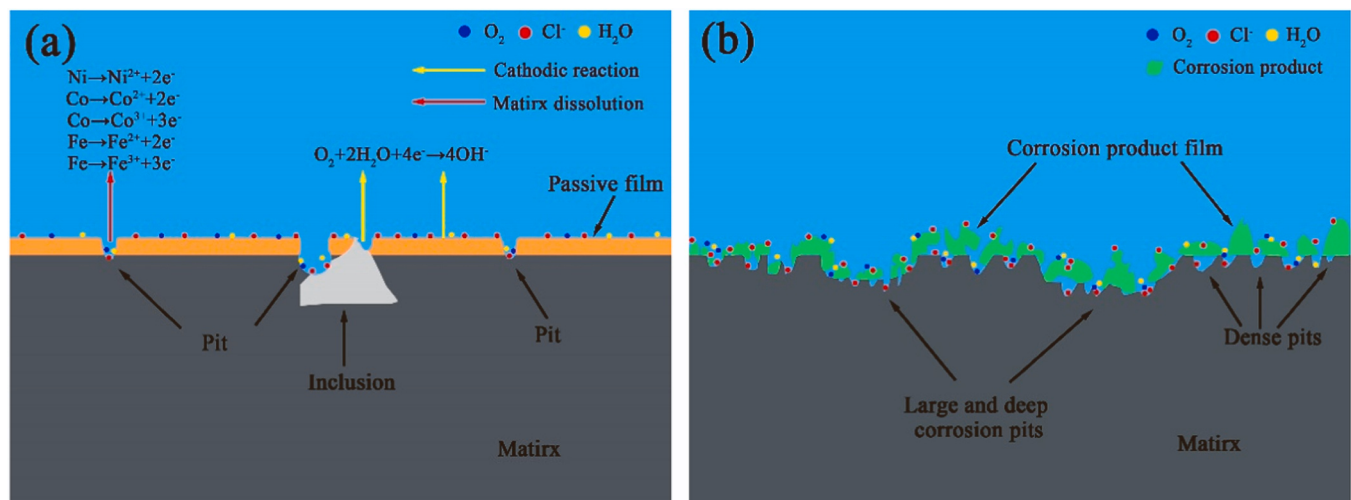
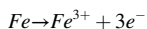
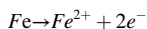
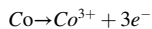
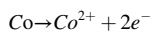
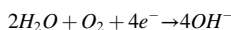


Fig. 17. Corrosion mechanism diagram of FeCoNi HEA (a) and X100 steel (b).



Cathodic reaction on the cathodic inclusion:



#### 4. Corrosion mechanism

Known from the above results, there is a significant difference in corrosion behavior of FeCoNi HEA and X100 steel in the simulated Golmud soil environment, and the corrosion mechanism is proposed in Fig. 17. Clearly, according to the polarization curve (Fig. 4) and corrosion morphology (Fig. 10) X100 steel displays the marked activation characteristic, while the spontaneous passivation occurs on the surface of the HEA. Moreover, the HEA experiences slight pitting corrosion, whereas the steel suffers severe general corrosion and the nonprotective and porous corrosion product film is formed on the surface of the steel. Therefore, the corrosion resistance of FeCoNi HEA is superior to X100 steel.

Based on the above analysis, the microstructure and surface film are the primary factors of different corrosion resistance of the two alloys. Firstly, FeCoNi HEA consists of a single FCC phase while multiple phases exist within X100 steel. Qi et al. [73] reported that multiphase pipeline steel easily formed micro-galvanic corrosion cells due to the potential difference between constituents, which promoted the occurrence of corrosion. Thus, the steel with multiple phases is easier to experience corrosion compared with single-phase HEA. Furthermore, the grain size of the HEA is much larger than the steel, which implies that the micro-galvanic corrosion between the internal grain and grain boundary of the HEA is weak. Hence, to a certain extent, large grain size can improve the corrosion resistance of the HEA. In addition, the compact, homogeneous and intact passive film indicated by the low carrier densities ( $N_D$  and  $N_A$ ), large  $R_f$  and the AFM topographic feature covering the HEA can significantly prevent the harmful ions from invading the substrate, which inhibits the matrix from corrosion. In contrast, the loose, porous and defective corrosion product film grown on the steel provides a great amount of channels for the permeation of harmful ions and molecules ( $\text{Cl}^-$ ,  $\text{H}_2\text{O}$ ,  $\text{O}_2$ ), which weakens the protective ability of the surface film and facilitates the corrosion of the steel matrix. Furthermore, as well known, the composition of the surface film largely determines its protection. For the HEA, it contains plentiful Ni element, which can form the corrosion-resistant oxide ( $\text{NiO}$ ) in its passive film, thus effectively enhancing the anti-corrosion property of the HEA [74], whereas the chemical composition of X100 steel is dominated by Fe element, which leads to produce a high content of iron-containing compound. Generally, its chemical stability is relatively lower than that of  $\text{NiO}$ , implying that the composition of the surface film results in the difference in corrosion resistance of the two alloys to some extent. Therefore, FeCoNi HEA possesses better anti-corrosion performance than X100 steel.

Additionally, the occurrence of pitting corrosion of the HEA is closely related to detrimental ions in test solution. Firstly, it is well known that chloride ion easily aggregates on the passive film of the HEA [75]. Due to its small volume and powerful diffusion ability, the adsorption of  $\text{Cl}^-$  often experiences in the defective area of the film. Subsequently, a series of chemical reactions occur between passive film and  $\text{Cl}^-$ , which thins the passive film thickness and causes partial destruction of the film. Meanwhile, the aggressive chloride ion absorbs into surface oxygen vacancy to replace oxygen, which produces cationic vacancies [76]. Thus, the high content of  $\text{Cl}^-$  in test solution causes an increase in the

number of defects in passive film, facilitating the dissolution of the HEA matrix. Furthermore, the ionization of  $\text{HCO}_3^-$  generates hydrogen ion (Eq. 7), which easily assembles in the active points and defect positions of passive film, then the ion of  $\text{H}^+$  causes a strong dissolution effect on the oxides and hydroxides within the film [77]. This significantly damages the film compactness, accelerates charge transfer and induces the pitting nucleation [78]. Moreover, the aggregation of harmful ions ( $\text{Cl}^-$  and  $\text{H}^+$ ) may cause the potential difference between different regions of passivation film, which is beneficial to the formation of micro-galvanic corrosion cell. This leads to the weakening of the film protection and acceleration of anodic dissolution, which improves the pitting sensitivity of the HEA.



#### 5. Conclusions

This paper comprehensively analyzed the difference in the corrosion resistance of FeCoNi HEA and X100 pipeline steel in a simulated alkaline soil environment. The following conclusions can be drawn:

1. FeCoNi HEA possesses superior corrosion resistance than X100 pipeline steel indicated by lower corrosion rate, passive current density ( $i_p$ ) and larger charge transfer resistance ( $R_{ct}$ ).
2. The difference in anti-corrosion property between FeCoNi HEA and X100 pipeline steel is closely correlated to the microstructure and structural stability of surface film. Loose, porous and uneven corrosion product film covering the surface of X100 steel cannot effectively prevent the matrix from corrosion. In contrast, the passive film of the HEA with complete, homogeneous and compact structure improves the protective ability of the HEA against corrosion.
3. FeCoNi HEA suffers slight pitting corrosion, while severe general corrosion is experienced on the surface of X100 pipeline steel.
4. For the HEA, due to the appearance of inclusion within the HEA, the micro-galvanic corrosion cell between the substrate and the inclusion enhances the corrosion of the HEA. Moreover, the main selected dissolution of Ni element is occurred in the matrix of the HEA.

#### CRediT authorship contribution statement

**Qihang Ni:** Writing – original draft, Investigation, Formal analysis, Data curation. **Min Zhu:** Writing – review & editing, Supervision, Methodology, Investigation, Formal analysis, Data curation, Conceptualization. **Shaoyi Guo:** Resources, Investigation. **Yongfeng Yuan:** Resources, Investigation.

#### Declaration of Competing Interest

The authors declare that they have no known competing financial interests or personal relationships that could have appeared to influence the work reported in this paper.

#### Data Availability

Data will be made available on request.

#### Acknowledgements

This work was supported by the National Natural Science Foundation of China (No. 51871026), and the Fundamental Research Funds of Zhejiang Sci-Tech University of China (No.22242293-Y).

#### References

- [1] J.W. Yeh, S.K. Chen, S.J. Lin, Nanostructured high-entropy alloys with multiple principal elements novel alloy design concepts and outcomes, *Adv. Eng. Mater.* 65 (2004) 299–303.

- [2] G. Qin, R.R. Chen, H.T. Zheng, Strengthening FCC-CoCrFeMnNi high entropy alloys by Mo addition, *J. Mater. Sci. Technol.* 354 (2019) 578–583.
- [3] G. Laplanche, A. Kostka, C. Reinhart, Reasons for the superior mechanical properties of medium-entropy CrCoNi compared to high-entropy CrMnFeCoNi, *Acta Mater.* 218 (2017) 292–303.
- [4] X.L. An, H. Zhao, C.L. Chu, T. Dai, T. Lu, Z.H. Huang, C. Guo, P.K. Chu, Hall-Petch relationship and corrosion behavior of cold-rolled CoNiFe medium entropy alloy, *J. Alloy. Compd.* 807 (2019) 151698.
- [5] S. Yoshida, T. Ikeuchi, T. Bhattacharjee, Y. Bai, A. Shibata, N. Tsuji, Effect of elemental combination on friction stress and Hall-Petch relationship in face-centered cubic high /medium entropy alloys, *Acta Mater.* 171 (2019) 201–215.
- [6] G. Laplanche, P. Gadaud, O. Horst, F. Otto, G. Eggeler, E.P. George, Temperature dependencies of the elastic moduli and thermal expansion coefficient of an equiatomic, single-phase CoCrFeMnNi high-entropy alloy, *J. Alloy. Compd.* 623 (2015) 348–353.
- [7] X.L. An, H. Zhao, T. Dai, H.G. Yu, Z.H. Huang, C. Guo, Paul K. Chu, C.L. Chu, Effects of heat treatment on the microstructure and properties of cold-forged CoNiFe medium entropy alloy, *Intermetallics* 110 (2019) 106477.
- [8] H.Q. Qu, Y. Ma, X.L. Li, Y.H. Duan, Y. Li, F. Liu, B. Yu, M.G. Tian, Z.J. Li, Y.Q. Yu, B. Li, Z.G. Lv, L. Wang, Ternary alloy (FeCoNi) nanoparticles supported on hollow porous carbon with defects for enhanced oxygen evolution reaction, *J. Colloid Interf. Sci.* 645 (2023) 107–114.
- [9] M.H. Tsai, Physical properties of high entropy alloys, *Entropy* 15 (2013) 5338–5345.
- [10] Z. Wu, H. Bei, G.M. Pharr, E.P. George, Temperature dependence of the mechanical properties of equiatomic solid solution alloys with face-centered cubic crystal structures, *Acta Mater.* 81 (2014) 428–441.
- [11] P.P. Li, A.D. Wang, C.T. Liu, Composition dependence of structure, physical and mechanical properties of FeCoNi(MnAl)<sub>x</sub> high entropy alloys, *Intermetallics* 87 (2017) 21–26.
- [12] T.T. Zuo, R.B. Li, X.J. Ren, Y. Zhang, Effects of Al and Si addition on the structure and properties of CoFeNi equal atomic ratio alloy, *J. Magn. Magn. Mater.* 371 (2014) 60–68.
- [13] L. Aval, Y. Shuhei, P. Jesada, I. Shiro, C. Yan, S. Hikaru, T. Nobuhiro, M. Mitsuhiro, Yield and flow properties of ultra-fine, fine, and coarse grain microstructures of FeCoNi equiatomic alloy at ambient and cryogenic temperatures, *Scr. Mater.* 230 (2023) 115392.
- [14] K.K. Halyna, S. Oleksandr, Z. Olha, H. Myroslava, S. Lesya, T.B. Ivan, S. Petro, Substantiation of the critical structural and mechanical state of low-alloy heat-resistant steel from steam pipelines of thermal power plant, *Eng. Fail. Anal.* 150 (2023) 107359.
- [15] L.Z. Xu, G.Y. Qiao, X. Gong, Y. Gu, K. Xu, F.R. Xiao, Effect of through-thickness microstructure inhomogeneity on mechanical properties and strain hardening behavior in heavy-wall X70 pipeline steels, *J. Mater. Res. Technol.* 25 (2023) 4216–4230.
- [16] H.P. Peng, Y.F. Gu, Q.W. Wang, J.X. Li, Y.G. Zhao, C.J. Wu, X.P. Su, Z.W. Li, Effect of Ti addition on mechanical properties and corrosion resistance of X80 pipeline steel, *Int. J. Ves. Pip.* (2023) 105003.
- [17] N.K. Waris, C. Rahul, Effect of filler metal on solidification, microstructure and mechanical properties of dissimilar super duplex/pipeline steel GTA weld, *Mat. Sci. Eng. A* 803 (2021) 140476.
- [18] T.T. Shun, L.Y. Chang, M.H. Shiu, Age-hardening of the CoCrFeNiMo<sub>0.85</sub> high-entropy alloy, *Mater. Char.* 81 (2013) 92–96.
- [19] A. Shabani, M.R. Toroghinejad, A. Shafyei, R.E. Logeb, Evaluation of the mechanical properties of the heat treated FeCrCuMnNi high entropy alloy, *Mater. Chem. Phys.* 221 (2019) 68–77.
- [20] L.H. Wen, H.C. Kou, J.S. Li, H. Chang, X.Y. Xue, L. Zhou, Effect of aging temperature on microstructure and properties of AlCoCrCuFeNi high-entropy alloy, *Intermetallics* 17 (2009) 266–269.
- [21] Z.G. Zhu, K.H. Ma, X. Yang, C.H. Shek, Annealing effect on the phase stability and mechanical properties of (FeNiCrMn)(100-x)Cox high entropy alloys, *J. Alloy. Compd.* 695 (2017) 2945–2950.
- [22] C.W. Lu, Y.S. Lu, Z.H. Lai, H.W. Yen, Y.L. Lee, Comparative corrosion behavior of Fe50Mn30Co10Cr10 dual-phase high-entropy alloy and CoCrFeMnNi high-entropy alloy in 3.5 wt% NaCl solution, *J. Alloy. Compd.* 842 (2020) 155824.
- [23] C.H. Tsau, S.X. Lin, C.H. Fang, Microstructures and corrosion behaviors of FeCoNi and CrFeCoNi equimolar alloys, *Mater. Chem. Phys.* 186 (2017) 534–540.
- [24] F.F. Eliyan, E.S. Mahdi, A. Alfantazi, Electrochemical evaluation of the corrosion behaviour of API-X100 pipeline steel in aerated bicarbonate solutions, *Corros. Sci.* 58 (2012) 181–191.
- [25] I.M. Galadza, A. Alfantazi, Electrochemical behavior of API-X100 pipeline steel in NS4, near-neutral, and mildly alkaline pH simulated soil solutions, *Corros. Sci.* 82 (2014) 45–57.
- [26] L.K. Ji, H.Y. Chen, H.L. Gao, H.L. Li, C.J. Zhuang, S.T. Gong, W.Z. Zhao, Key issues in the specification of high strain line pipe used in strain-based designed districts of the 2nd west to east pipeline, in: Proceedings of IPC2008, Calgary, Alberta, Canada, (2008) 695–703.
- [27] R.X. He, H.J. Jin, Permafrost and cold-region environmental problems of the oil product pipeline from Golmud to Lhasa on the Qinghai-Tibet Plateau and their mitigation, *Cold Reg. Sci. Technol.* 64 (2010) 279–288.
- [28] L.N. Duan, Y. Chen, Q.Y. Liu, S.J. Jia, C.C. Jia, Microstructures and mechanical properties of X100 pipeline steel strip, *J. Iron Steel Res.*, Int. 21 (2014) 227–232.
- [29] F.F. Eliyan, F. Lcre, A. Alfantazi, Passivation of HAZs of API-X100 pipeline steel in bicarbonate-carbonate solutions at 298 K, *Mater. Corros.* 65 (2013) 1162–1171.
- [30] Z.B. Ga, D. Wang, J.T. Jiang, J.Y. He, Y. Wang, F. Xie, Effects of magnetic field on corrosion behaviour of X100 pipeline steel in simulated soil solution containing sulphate-reducing bacteria, *Int. J. Electrochem. Sci.* 16 (2021) 211247.
- [31] C.Q. Fu, Z.D. Xie, Corrosion behavior of X100 steel heat-affected zone in acidic soil solution, *Int. J. Electrochem. Sci.* 17 (2022) 220234.
- [32] Y. Yang, M. Sun, Y.L. Luo, W.G. Zeng, R.Y. He, Effects of alternating current on corrosion behavior of X100 pipeline steel in simulated soil solution, *Int. J. Electrochem. Sci.* 16 (2021) 150927.
- [33] X.H. Wang, Y. Yong, Y.C. Chen, H.T. Wang, K.L. Wei, Corrosion behavior of X100 pipeline steel and its heat-affected zones in simulated alkaline soil solution, *Int. J. Electrochem. Sci.* 14 (2019) 9181–9192.
- [34] M. Zhu, J. Ma, Y.F. Yuan, S.Y. Guo, Effect of AC interference on corrosion behavior of X100 pipeline steel with different microstructure in alkaline soil environment, *Int. J. Electrochem. Sci.* 14 (2019) 9711–9725.
- [35] H.Q. Qu, Y.R. Ma, X.L. Li, Y.H. Duan, Y. Li, F. Liu, B. Yu, M.G. Tian, Z.J. Li, Y.Q. Yu, B. Li, Z.G. Lv, L. Wang, Ternary alloy (FeCoNi) nanoparticles supported on hollow porous carbon with defects for enhanced oxygen evolution reaction, *J. Colloid Interf. Sci.* 645 (2023) 107–114.
- [36] S.X. Cheng, R.S. Lv, F. Cheng, B. Han, A.Q. Fu, X.Y. Zhang, J.X. Zhang, Y.R. Feng, H.L. Gao, Microstructure and properties of X100 large-deformability pipeline steel based on heating on-line partitioning, *Mater. Today Commun.* 35 (2023) 105771.
- [37] Q.C. Zhao, Z.M. Pan, X.F. Wang, H. Luo, Y. Liu, X.G. Li, Corrosion and passive behavior of Al<sub>x</sub>CrFeNi<sub>3-x</sub> (x = 0.6, 0.8, 1.0) eutectic high entropy alloys in chloride environment, *Corros. Sci.* 208 (2022) 110666.
- [38] L.J. Chen, W. Liu, B.J. Dong, Y.G. Zhao, T.Y. Zhang, Y.M. Fan, W.J. Yang, Insight into electrochemical passivation behavior and surface chemistry of 2205 duplex stainless steel: effect of tensile elastic stress, *Corros. Sci.* 193 (2021) 109903.
- [39] Y.Z. Shi, L. Collins, R. Feng, C. Zhang, N. Balke, P.K. Liaw, B. Yang, Homogenization of Al<sub>x</sub>CoCrFeNi high-entropy alloys with improved corrosion resistance, *Corros. Sci.* 133 (2018) 120–131.
- [40] T. Thublaor, A. Khemphet, N. Jungjatuporn, et al., Effect of cleaning solution on corrosion resistance of AISI 304 austenitic stainless steel in railway industry, *Mater. Today.: Proc.* 52 (2022) 2512–2516.
- [41] M. Zhu, Q. Zhang, Y. Yuan, Study on the correlation between passive film and AC corrosion behavior of 2507 super duplex stainless steel in simulated marine environment, *J. Electroanal. Chem.* 864 (2020) 114072.
- [42] X.W. Qiu, Y.P. Zhang, C.G. Liu, Effect of Ti content on structure and properties of Al<sub>2</sub>CrFeNiCoCuTi<sub>x</sub> high-entropy alloy coatings, *J. Alloy Compd.* 585 (2014) 282–286.
- [43] H. Luo, X.Z. Wang, C.F. Dong, et al., Effect of cold deformation on the corrosion behavior of UNS S31803 duplex stainless steel in simulated concrete pore solution, *Corros. Sci.* 124 (2017) 178–192.
- [44] D.C. Kong, C.F. Dong, X.Q. Ni, Mechanical properties and corrosion behavior of selective laser melted 316L stainless steel after different heat treatment processes, *J. Mater. Sci. Technol.* 35 (2019) 1499–1507.
- [45] N.A. Ravindranath, P.C. Clinsha, R. Pandian, G. Natarajan, A. Bahuguna, A.S. N. Sivaraman, K.I. Gnanasekar, Polarization resistance of Pt/YSZ and ITO/YSZ interfaces in multilayered Pt|YSZ|Pt and ITO|YSZ|ITO thin films, *Surf. Interfaces* 37 (2023) 102700.
- [46] A. Nishikata, Y. Ichihara, T. Tsuru, An application of electrochemical impedance spectroscopy to atmospheric corrosion study, *Corros. Sci.* 37 (1995) 897–911.
- [47] J.J. Shi, Y.Q. Zou, J. Ming, Effect of DC stray current on the electrochemical behavior of low-carbon steel and 10% Cr steel in saturated Ca(OH)<sub>2</sub> solution, *Corros. Sci.* 169 (2020) 108610.
- [48] H.X. Wan, D.D. Song, X.L. Shi, Y. Cai, T.T. Li, C.F. Chen, Corrosion behavior of Al<sub>0.4</sub>CoCu<sub>0.6</sub>NiSi<sub>0.2</sub>Ti<sub>0.25</sub> high-entropy alloy coating via 3D printing laser cladding in a sulphur environment, *J. Mater. Sci. Technol.* 60 (2021) 197–205.
- [49] Q.C. Zhao, Z.M. Pan, X.F. Wang, H. Luo, Y. Liu, X.G. Li, Corrosion and passive behavior of Al<sub>x</sub>CrFeNi<sub>3-x</sub> (x = 0.6, 0.8, 1.0) eutectic high entropy alloys in chloride environment, *Corros. Sci.* 208 (2022) 110666.
- [50] H.C. Tian, X.Q. Cheng, Y. Wang, et al., Effect of Mo on interaction between a/g phases of duplex stainless steel, *Electrochim. Acta* 267 (2018) 255–268.
- [51] F. Hao, H. Li, X. Wu, et al., Effect of nitrogen on corrosion behaviour of a novel high nitrogen medium-entropy alloy CrCoNiN manufactured by pressurized metallurgy, *J. Mater. Sci. Technol.* 34 (2018) 1781–1790.
- [52] H. Luo, S.W. Zou, Y.H. Chen, et al., Influence of carbon on the corrosion behavior of interstitial equiatomic CoCrFeMnNi high-entropy alloys in a chlorinated concrete solution, *Corros. Sci.* 163 (2020) 108287.
- [53] G. Brug, A.L. van den Eeden, M. Sluyters-Rehbach, J.H. Sluyters, The analysis of electrode impedances complicated by the presence of a constant phase element, *J. Electroanal. Chem. Interfacial Electrochem* 176 (1984) 275–295.
- [54] M. Sanchez, J. Gregori, C. Alonso, et al., Electrochemical impedance spectroscopy for studying passive layers on steel rebars immersed in alkaline solutions simulating concrete pores, *Electrochim. Acta* 52 (2007) 7634–7641.
- [55] F. Mao, C. Dong, S. Sharifi-Asl, Passivity breakdown on copper: Influence of chloride ion, *Electrochim. Acta* 144 (2014) 391–399.
- [56] C.A. Gervasi, M.E. Folquer, A.E. Vallejo, P.E. Alvarez, Electron transfer across anodic films formed on tin in carbonate-bicarbonate buffer solution, *Electrochim. Acta* 50 (2005) 1113–1119.
- [57] E. Rahimi, A. Kosari, S. Hosseinpour, A. Davoodi, H. Zandbergen, J.M.C. Mol, Characterization of the passive layer on ferrite and austenite phases of super duplex stainless steel, *Appl. Surf. Sci.* 496 (2019) 143634.
- [58] N.E. Hakiki, Comparative study of structural and semiconducting properties of passive films and thermally grown oxides on AISI 304 stainless steel, *Corros. Sci.* 53 (2011) 2688–2699.

- [59] N.B. Hakiki, S. Boudin, B. Rondot, M. Da Cunha Belo, The electronic structure of passive films formed on stainless steels, *Corros. Sci.* 37 (1995) 1809–1822.
- [60] Y. Zhang, H. Luo, Q. Zhong, H. Yu, J. Lv, Characterization of passive films formed on As-received and sensitized AISI 304 stainless steel, *Chin. J. Mech. Eng.* 32 (1) (2019) 27.
- [61] Z.M. Pan, H. Luo, Q.C. Zhao, H.X. Cheng, Y. Wei, X.F. Wang, B.W. Zhang, X.G. Li, Tailoring microstructure and corrosion behavior of CoNiVAI<sub>x</sub> medium entropy alloys via Al addition, *Corros. Sci.* 207 (2022) 110570.
- [62] H.X. Cheng, H. Luo, X.F. Wang, Z.M. Pan, Y. Jiang, X.G. Li, Electrochemical corrosion and passive behavior of a new high-nitrogen austenitic stainless steel in chloride environment, *Mater. Chem. Phys.* 292 (2022) 126837.
- [63] H. Luo, X.Z. Wang, C.F. Dong, et al., Effect of cold deformation on the corrosion behavior of UNS S31803 duplex stainless steel in simulated concrete pore solution, *Corros. Sci.* 124 (2017) 178–192.
- [64] J.H. Wang, D.G. Li, T.M. Shao, Diffusivity of point defects in the passive film on a Ni<sub>16</sub>Cr<sub>13</sub>Co<sub>4</sub>Mo alloy in molten NaCl-Na<sub>2</sub>SO<sub>4</sub>, *Corros. Sci.* 223 (2023) 111456.
- [65] D.D. Macdonald, The history of the point defect model for the passive state: a brief review of film growth aspects, *Electrochim. Acta* 56 (2011) 1761–1772.
- [66] C. Chao, L. Lin, D. Macdonald, A point defect model for anodic passive films: I. Film growth kinetics, *J. Electrochem. Soc.* 128 (1981) 1187–1194.
- [67] V.A. Katkar, G. Gunasekaran, A.G. Rao, Effect of the reinforced boron carbide particulate content of AA6061 alloy on formation of the passive film in seawater, *Corros. Sci.* 53 (2021) 2700–2712.
- [68] K.K. Cui, H.B. Mao, Y.Y. Zhang, J. Wang, F.Q. Shen, Microstructure and corrosion behavior of Al<sub>2</sub>O<sub>3</sub>–Cr<sub>2</sub>O<sub>3</sub> composites with various Cr<sub>2</sub>O<sub>3</sub> content in Al<sub>2</sub>O<sub>3</sub>–SiO<sub>2</sub>–CaO–FeO slag, *Ceram. Int.* 48 (2022) 35555–35567.
- [69] T. Bellezze, G. Giuliani, A. Viceré, G. Roventi, Study of stainless steels corrosion in a strong acid mixture. Part 2: anodic selective dissolution, weight loss and electrochemical impedance spectroscopy tests, *Corros. Sci.* 130 (2018) 12–21.
- [70] M. Zhu, B.Z. Zhao, Y.F. Yuan, S.Y. Guo, Y.B. Chen, G.T. Zhu, Study on the corrosion behavior of CoCrFeMnNi HEA in NH<sub>4</sub>Cl solutions with different concentrations, *J. Mater. Eng. Perform.* 32 (2023) 4109–4123.
- [71] H. Luo, S.W. Zou, Y.H. Chen, Z.M. Li, C.W. Du, X.G. Li, Influence of carbon on the corrosion behaviour of interstitial equiatomic CoCrFeMnNi high-entropy alloys in a chlorinated concrete solution, *Corros. Sci.* 163 (2020) 108287.
- [72] Z.Y. Cui, S.S. Chen, Y.P. Dou, S.K. Han, L.W. Wang, C. Man, X. Wang, S.G. Chen, Y. F. Cheng, X.G. Li, Passivation behavior and surface chemistry of 2507 super duplex stainless steel in artificial seawater: influence of dissolved oxygen and pH, *Corros. Sci.* 150 (2019) 218–234.
- [73] X.N. Qi, P.C. Huan, X.M. Chen, X.N. Wang, Z.G. Liu, X.J. Shen, H.S. Di, Corrosion resistance and mechanism of X100 pipeline steel laser-metal active gas hybrid welds with Cr containing welding wire in NS4 solution, *Corros. Sci.* 221 (2023) 111329.
- [74] M. Zhu, B.Z. Zhao, Y.F. Yuan, S.M. Yin, S.Y. Guo, G.Y. Wei, Effect of annealing temperature on microstructure and corrosion behavior of CoCrFeMnNi high-entropy alloy in alkaline soil simulation solution, *Mater. Chem. Phys.* 279 (2022) 125725.
- [75] A. Sundar, G.L. Chen, L. Qi, Substitutional adsorptions of chloride at grain boundary sites on hydroxylated alumina surfaces initialize localized corrosion, *npj Mat. Degrad.* 5 (2021) 18.
- [76] L. Sun, T.Y. Zhao, J. Qiu, Y.T. Sun, K.J. Li, H.B. Zheng, Y.M. Jiang, Y.H. Li, J. Li, W. H. Li, D.D. Macdonald, Point defect model for passivity breakdown on hyper-duplex stainless steel 2707 in solutions containing bromide at different temperatures, *Corros. Sci.* 194 (2022) 109959.
- [77] J.Y. Li, X.K. Zhong, T.G. Wang, T. Shang, J.Y. Hu, Z. Zhang, D.Z. Zeng, D. Hou, T. H. Shi, Synergistic effect of erosion and hydrogen on properties of passive film on 2205 duplex stainless steel, *J. Mater. Sci. Technol.* 67 (2021) 1–10.
- [78] W. Wu, Y. Pan, Z.Y. Liu, C.W. Du, X.G. Li, Electrochemical and stress corrosion mechanism of submarine pipeline in simulated seawater in presence of different alternating current densities, *Metals* 11 (2018) 1074.